

TuneS: Patient-specific model-based optimization of contact configuration in deep brain stimulation

Anna F. Frigge *Graduate Student Member, IEEE*, Lina Uggla, Elena Jiltsova, Markus Fahlström, Dag Nyholm, and Alexander Medvedev *Member, IEEE*

Abstract—Objective: The objective of this study is to develop and evaluate a systematic approach to optimize Deep Brain Stimulation (DBS) parameters, addressing the challenge of identifying patient-specific settings and optimal stimulation targets for various neurological and mental disorders. **Methods:** TuneS, a novel pipeline to predict clinically optimal DBS contact configurations based on predefined targets and constraints, is introduced. The method relies upon patient-specific models of stimulation spread and extends optimization beyond traditional neural structures to include automated, model-based targeting of streamlines. **Results:** Initial findings demonstrate that STN motor streamlines consistently receive a significant portion of the allocated stimulation volume, suggesting that a consistent portion of the stimulation should ideally focus on the STN motor streamlines. At the example of a small cohort of Parkinson's disease patients, the value of model-based contact predictions for assessing stimulation targets while observing constraints is demonstrated. **Conclusion:** TuneS shows promise as a research tool, enabling systematic assessment of DBS target effectiveness and facilitating constraint-aware optimization of stimulation parameters. **Significance:** The presented pipeline offers a pathway to improve patient-specific DBS therapies and contributes to the broader understanding of effective DBS targeting strategies.

Index Terms—Computational modeling, Deep Brain Stimulation, Optimization, Parkinson's Disease

I. INTRODUCTION

Deep Brain Stimulation (DBS) has emerged as a powerful and cost-efficient [1] therapeutic tool for addressing a range of neurological and mental disorders. In DBS, stimulation electrodes are implanted into specific areas of the brain to chronically deliver controlled electrical impulses. The precise DBS target area varies depending on the disorder and is selected based on the patient's specific symptoms. A typical DBS target is the subthalamic nucleus (STN) due to its significant role in alleviating symptoms across various disorders with distinct symptoms [2]–[5]. Despite the effectiveness of DBS in the alleviation of symptoms, optimizing stimulation parameters in clinical practice relies on a trial-and-error method called monopolar review, which involves testing each contact, one at a time, with monopolar stimulation. This process is laborious and time-consuming, often resulting in suboptimal clinical outcomes due to the time constraints faced by clinical staff [6] and wide inter-patient variability of optimal

stimulation settings evidenced in numerous studies. Moreover, the evolution of increasingly sophisticated lead designs has provided clinicians with enhanced control over the distribution of the electric field, while simultaneously increasing the complexity associated with parameter optimization.

In recent years, there has been an on-going effort to develop automated programming algorithms that can aid clinicians in the programming procedure. These include image guided algorithms [7], [8], data-driven approaches utilizing monopolar review data [9], and algorithms that incorporate quantified symptoms, e.g. tremor measurements via smartwatch applications [10], or other biomarkers like beta activity in local field potentials (LFP) [11] or cortical evoked potentials [12].

Recent studies have shown that image-guided tools, which display the DBS lead relative to key target structures, can reduce initial programming times by providing a useful starting point for clinicians [13]. Additionally, some lead manufacturers offer commercial software for image-guided parameter predictions as part of their DBS systems, which have demonstrated improved clinical outcomes in Parkinson's Disease (PD) patients [14]. Shub *et al.* [8] found that predictions made by GuideXT[®] did not always align with decisions taken by clinical programmers, yet resulted in significant symptom relief. However, commercial software solutions often provide limited flexibility for individual target selection, constraint customization, and parameter adjustments, which restricts their utility as research tools. Additionally, these platforms typically lack functionality for exporting results to other software for further analysis or processing, thus impeding their integration into broader research workflows.

While data-driven algorithms can be valuable for making predictions, they often fail to provide insights into the underlying mechanisms of DBS. Moreover, these methods frequently struggle with extrapolation, which is particularly challenging in DBS due to the highly individualized nature of the therapy. Additionally, differences in procedures between medical centers, limited data for less common DBS-treated disorders, and the complexity of assessing a patient's overall condition further complicate the use of data-driven approaches.

Algorithms based on kinematic biomarkers or LFP beta activity are generally applicable only to patients who exhibit these specific biomarkers, limiting their utility. Additionally, many of these tools primarily focus on motor improvements, potentially overlooking the importance of avoiding stimulation in areas that could cause non-motor side effects.

To address these challenges, an automated image-guided programming pipeline called TuneStim (TuneS)¹ has been developed at Uppsala University in collaboration with Uppsala University Hospital aimed at predicting initial DBS configuration settings that can be further refined by clinical practitioners. Leveraging readily available medical imaging data from routine clinical procedures, such as preoperative magnetic resonance imaging (MRI) and postoperative computed tomography (CT) scans, TuneS facilitates offline computations. The user can select the relevant target structures, including specific anatomical brain regions and results derived from fiber

This paragraph of the first footnote will contain the date on which you submitted your paper for review. This work is funded by the Swedish Research Council via Grant 2020-02901 to the project "Patient-specific dynamical modeling and optimization of deep brain stimulation" within The EU Joint Programme – Neurodegenerative Disease Research.

A. F. Frigge is with the Department of Information Technology, Uppsala University, Sweden (e-mail: anna.frigge@it.uu.se).

L. Uggla, was with the Department of Information Technology, Uppsala University, Sweden. She is now with Stardots AB, Uppsala, Sweden (e-mail: lina.uggla@stardots.se).

E. Jiltsova is with the Department of Medical Sciences, Neurosurgery, Uppsala University, Sweden (e-mail: elena.jiltsova@neuro.uu.se).

M. Fahlström is with the Department of Surgical Sciences, Uppsala University, Sweden (e-mail: markus.fahlstrom@uu.se).

D. Nyholm is with the Department of Medical Sciences, Neurology, Uppsala University, Sweden (e-mail: dag.nyholm@neuro.uu.se).

A. Medvedev is with the Department of Information Technology, Uppsala University, Sweden (e-mail: alexander.medvedev@it.uu.se).

¹TuneS is freely available on github.com/annafrigge/TuneStim.

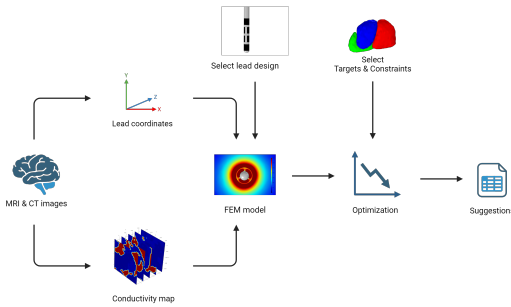


Fig. 1: TuneS schematic workflow based on preoperative MRI and postoperative CT images [15].

tractography. To distinguish between actual anatomical fibers and those reconstructed using fiber tractography from Diffusion Tensor Imaging (DTI), the term *streamlines* will be used throughout this paper to specifically refer to the reconstructed tracts. The computed settings can then be seamlessly integrated into patient consultations, streamlining and expediting the programming process. A schematic illustration of the workflow in TuneS is given in Fig. 1.

This paper highlights the following key contributions:

- 1) Research tool: TuneS is a freely available software and holds potential as a research tool for investigating relationships between stimulating different DBS targets and constrained regions on the one hand, and therapeutic outcomes and stimulation-induced side-effects on the other hand.
- 2) Streamline targeting: TuneS offers the option to target streamlines, rather than relying solely on traditional anatomical targets. To the best of our knowledge, this is the first time automated optimization-based contact predictions in DBS have been extended to include streamline targeting.

Besides PD, DBS is utilized in treating other neurological disorders, Essential Tremor, Dystonia, drug-resistant Epilepsy, as well as various mental disorders e.g. Obsessive Compulsive Disorder (OCD), Depression, Tourette's syndrome and other conditions. While TuneS is suitable for simulating different targets and predict optimal contact configurations in all the disorders treated with DBS, the findings presented in this paper solely pertain to PD patients with STN DBS. The presented results are clinically relevant, yet a relatively simple application was chosen to demonstrate the feasibility of TuneS.

This paper presents the steps constituting the process of obtaining stimulation configuration suggestions with TuneS and the validation of the developed software on a cohort of ten PD patients treated at Uppsala University Hospital.

II. METHODOLOGY

A. Patient cohort

The workflow of the TuneS is validated at a cohort of ten Parkinson's disease patients who underwent DBS surgery at Uppsala University Hospital². The STN was selected as the surgical target for all patients, with nine receiving bilateral DBS and one undergoing unilateral DBS, resulting in a total of 19 leads. Half of the patients were implanted with the Boston Vercise CartesiaTM Directional Lead, while the other half were implanted with the Abbot's St. Jude Medical InfinityTM Directional Lead as depicted in Fig. 2.

For each patient, preoperative T1- and T2-weighted MRI, as well as post-operative CT images acquired during routine clinical procedures,

²The study was approved by the Swedish Ethics Review Authority, Registration number 2019-05718, and all participants gave informed written consent prior to the beginning of the study.

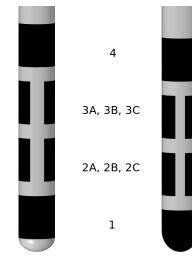


Fig. 2: Schematic illustration of the Boston Vercise CartesiaTM Directional Lead (left) and the Abbott's St. Jude Medical InfinityTM Directional Lead (right) with the contact labels used in this study. Note that the segmented contacts (A, B, C) are labeled in a clockwise direction.

were obtained. Although the timing of the CT scans post-surgery varied between patients, all images were visually checked for major air pockets that could potentially affect the reconstruction of the lead location relative to the stimulation targets.

B. Image processing

Pre-operative MRI (T1 and T2) as well as a post-operative CT images were co-registered and normalized using Lead DBS v2.6 [16]. The lead coordinates were then reconstructed using the PaCER algorithm [17]. Moreover, the DiODE algorithm [18] was applied to obtain the lead orientation based on the marker artifacts in the post-operative CT. While the latter algorithm has been validated for the Boston Vercise CartesiaTM Directional Lead, it has not been validated for the Abbott's St. Jude Medical InfinityTM Directional Lead.

C. TuneS

TuneS features a graphical interface as illustrated in Fig. 3. Implemented in MATLAB, the pipeline relies on dependencies including SPM12, Lead-DBS v2.6 [16] or v3.0 [19], and COMSOL Multiphysics[®] with LiveLinkTM for MATLAB.

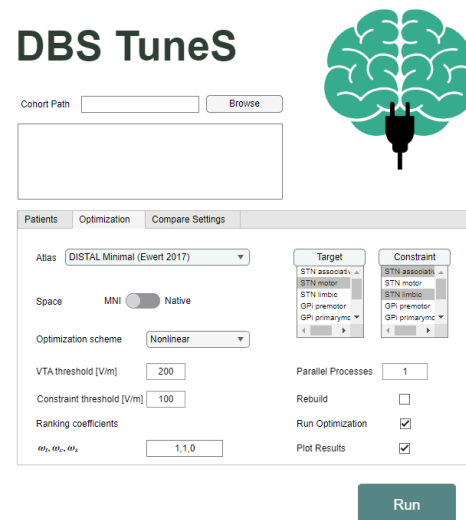


Fig. 3: Graphical user interface of TuneS, enabling patient cohort processing, individual target and constraint selection, and model parameter modification.

a) *FEM model*: The FEM model is built in COMSOL Multiphysics[®] using LiveLinkTM for MATLAB. Currently, TuneS features four lead designs, including the Abbot's (St. Jude) Medical

Infinity™ Directional lead, the Boston Scientific Vercise Standard lead, the Boston Scientific Vercise Cartesia™ Directional lead, and the Medtronic 3887 lead.

Surrounding the chosen lead type, heterogeneous tissue is modeled in a 50 mm × 50 mm × 50 mm box. To account for the heterogeneous tissue properties in vicinity of the lead, a conductivity map is generated based on a segmentation of the 7 T ICBM 152 2009a Nonlinear Asymmetric T1 template MRI [20]. Further away from the lead, the tissue is modeled as homogeneous matter. The default conductivity values for gray matter (GM), white matter (WM), and cerebrospinal fluid (CSF), the encapsulation layer, and the homogeneous medium are $\sigma_{GM} = 0.09$ S/m, $\sigma_{WM} = 0.06$ S/m, $\sigma_{CSF} = 2.0$ S/m, $\sigma_{enc} = 0.18$ S/m, and $\sigma_{hom} = 0.1$ S/m, respectively.

The FEM model solves the quasi-static approximation of Maxwell's equation

$$\nabla \cdot (\sigma \nabla u) = 0, \quad (1)$$

where $\nabla \cdot$ is the divergence operator, σ denotes the conductivity, and ∇u stands for the gradient of the electric potential. All non-active contact surfaces were given a floating boundary condition.

The boundary condition on the active contacts is given by the surface integral

$$\int_{\partial\Omega} \mathbf{J} \cdot \mathbf{n} \, dS = I_0, \quad (2)$$

where \mathbf{J} represents the current density, \mathbf{n} is the normal vector to the contact surface, and I_0 is the constant current amplitude. The FEM model comprises approximately 1,200,000 elements, with slight variations depending on the lead type.

b) Optimization schemes: The effect of DBS on the neural tissue surrounding the lead is typically approximated by the volume of tissue activated (VTA). A point is assumed activated and therefore included in the VTA, if the electric field norm E at this point exceeds a specified threshold $E_{th,t}$. Exploiting the linearity of (1), the field obtained from the FEM model under a unit stimulus can be linearly scaled to obtain the results for different amplitudes. It is noteworthy that TuneS employs point clouds in calculating VTA rather than volumes. Targets and constraints are represented as disjoint sets, and when multiple targets or constraints are involved, the union of these disjoint sets defines the target volume Ω_t and the constraint volume Ω_c , respectively. In the following, the 3D point coordinates (x, y, z) of each point in Ω_t and Ω_c are mapped to the indices i and j , respectively, using a coordinate-to-index conversion. In this mapping, the innermost loop iterates through x , followed by y , and finally z . It is important to note that the point-wise optimization schemes presented below assume a uniform distribution of the target or constraint points in the respective volume.

Based on the above concept of tissue activation, the current version of the TuneS features multiple optimization schemes, two of which are presented in the following. The first one is a linear optimization scheme that aims to activate as many of the target points as possible while keeping the scaled electric field norm $\lambda \cdot E_j$ at θ % of points j within the constraint volume Ω_c under a specific constraint threshold value $E_{th,c}$. It can be written as

$$\begin{aligned} \max_{\lambda} \quad & \sum_i \lambda \cdot E_i \quad \forall i \in \Omega_t \\ \text{s.t.} \quad & \lambda \cdot E_j \leq E_{th,c} \quad \text{for } \theta \text{ \% of points } j \text{ in } \Omega_c, \end{aligned} \quad (3)$$

where λ is the stimulation amplitude and E_i denotes the electric field norm at the points i within the target volume Ω_t .

The second optimization scheme uses a nonlinear cost function that penalizes under-stimulation of target points quadratically, while overstimulation is penalized linearly, as proposed in [21]. It is given by

$$f_{cost,i} = \begin{cases} |\lambda \cdot E_i - E_{th,t}|^2 & \text{if } \lambda \cdot E_i \leq E_{th,t} \\ |\lambda \cdot E_i - E_{th,t}| & \text{if } \lambda \cdot E_i > E_{th,t} \end{cases}, \quad (4)$$

where $E_{th,t}$ denotes the desired target field strength and $|\cdot|$ represents the absolute value. Minimization of the cost function gives

$$\begin{aligned} \min_{\lambda} \quad & \sum_i f_{cost,i} \quad \forall i \in \Omega_t \\ \text{s.t.} \quad & \lambda \cdot E_j \leq E_{th,c} \quad \text{for } \theta \text{ \% of points } j \text{ in } \Omega_c. \end{aligned} \quad (5)$$

In the case of the eight-contact leads illustrated in Fig. 2, these optimization problems are solved for 31 different contact combinations, representing a clinically relevant subset of all possible configurations. In this paper, it is assumed that $E_{th,c} = 100$ and $E_{th,t} = 200$. In the following, a change in the constraint variable θ is mainly handled by introducing a constraint relaxation variable γ . Specifically, a relaxation of the constraint variable θ by γ indicates that the constraints in (3) and 5 are satisfied for $\theta = 100 - \gamma$ percent of the points in Ω_c .

Optimization problem (3) is solved using MATLAB's `linprog`, whereas the minimization of the cost function in (5) is handled by `fmincon`.

c) Targets and constraints: The selection of stimulation target and constraint areas is left to the user as it may vary between different disorders and is subject of on-going research. In this paper, TuneS was employed to investigate two potential target structures in DBS for PD: (1) the subdivisions of the STN [22] and (2) the STN streamlines [23], specifically the reconstructed hyperdirect pathways connecting STN subdivisions to corresponding cortical regions. The STN motor (respectively the STN motor streamlines) was considered as the stimulation target, while the STN limbic and STN associative regions (respectively their streamlines) were delineated as constraint areas.

Generally, STN streamlines consist of a much higher number of points, which span from the STN region all the way to the motor cortex. By removing points outside of the region of interest i.e. in the vicinity of the DBS lead, the number of points is reduced. Nevertheless, this method leads to relatively small target coverage percentages, depending on the size of the region of interest.

d) Configuration suggestions: The performance of active contact configurations can be ranked in various ways. In this study, the optimized settings for all contact configurations were ranked by a heuristic score S , defined as

$$S = \omega_t \cdot p_{act,t} - \omega_c \cdot p_{act,c} - \omega_s \cdot p_{act,s}, \quad (6)$$

where $p_{act,t}$ and $p_{act,c}$ represent the percentage of target and constraint activated, respectively. Additionally, $p_{act,s}$ denotes the percentage spill, i.e. the percentage of activated tissue outside the target region. The weights, ω_t , ω_c , and ω_s can be defined by the user from clinical preferences. When targeting streamlines, defining spill is a rather complex task due to the spaces between individual streamlines. Therefore, in this study, it was assumed that $\omega_t = 1$, $\omega_c = 1$, and $\omega_s = 0$. While exploring different ratios of these ranking coefficients is an important topic, it lies beyond the scope of this paper.

A comparison between two stimulation settings can be made in terms of VTA, target coverage, and constraint coverage. Provided that the electric field norm is calculated in the same system of coordinates, the overlap of two VTAs X and Y resulting from two different DBS settings, can be evaluated using the Dice-Sørensen coefficient, given by

$$D = \frac{|X \cap Y|}{|X| + |Y|}, \quad (7)$$

TABLE I: The clinically active contact configurations and current amplitudes for all patients.

Patient		Active contacts	I_0 [mA]
01	sin	2A,2B,2C	2.85
	dx	2A,2C	3.0
02	sin	2C	1.5
	dx	2B,2C,3B	4.6
03	sin	3A,3B,3C	4.6
	dx	3A,3B,3C	3.4
04	sin	2A,2B,2C	2.0
	dx	3A,3B,3C	2.6
05	sin	3B,3C,4	2.6
	dx	2A,2B,3A,3B	1.7
06	sin	2C	1.5
	dx	2B,3B	3.2
07	sin	3B,3C	3.0
	dx	2B,3C	1.2
08	sin	2A,2B,2C	3.3
	dx	3A,3B,3C	4.4
09	sin	-	-
	dx	2A	3.8
10	sin	C2A,C2B,C3A,C3B	4.2
	dx	2A,2B,2C	1.0

where $|\cdot|$ denotes the cardinality of a set.

e) *Clinical configurations:* When comparing the contact configurations suggested by TuneS to those used clinically, it is important to note that only a limited number of combinations can be tested in clinical practice. This is primarily due to time constraints faced by clinical staff and the variable time it takes for patients to experience the effects of a given setting, with some side effects potentially only emerging after several hours or days. Therefore, the clinically used configurations do not necessarily represent ground-truth, but rather serve as a reference point. A stimulation setting used clinically is also typically free of adverse side effects, which property corresponds, with respect to the considered optimization problems, to low values of constraint coverage.

III. RESULTS

All the computations have been performed in MNI space to facilitate inter-subject comparability.

A. Clinical Settings

The most recent clinically used settings for all patients including the active contacts and stimulation amplitude are summarized in Table I.

The target and constraint coverage for both the STN subdivisions and STN streamlines under these clinical settings were computed from the individualized FEM models and are presented in Fig. 4. The VTA threshold was adjusted according to the pulse width used clinically, following [24]. For the STN subdivisions, low target coverage was observed from the right lead of Patient 7 and from both leads of Patient 10. In Patient 3, both high target coverage and relatively high constraint coverage were noted, likely due to the higher stimulation amplitude used for this patient (4.6 mA). In Fig. 4b, results from a point-wise approach for streamline activation are presented, where only the portion of the streamlines in the region near the lead were considered and further treated as a point cloud. This method leads to relatively small target coverage percentages due to the large size of the region of interest. Alternatively, it can be assumed that the entire trajectory of the streamline is activated if any point along its path exceeds a specific field threshold. Results using this approach are shown in Fig. 4c. All but four of the clinical settings achieved a hundred percent target coverage, but also up to 90% of constraint coverage.

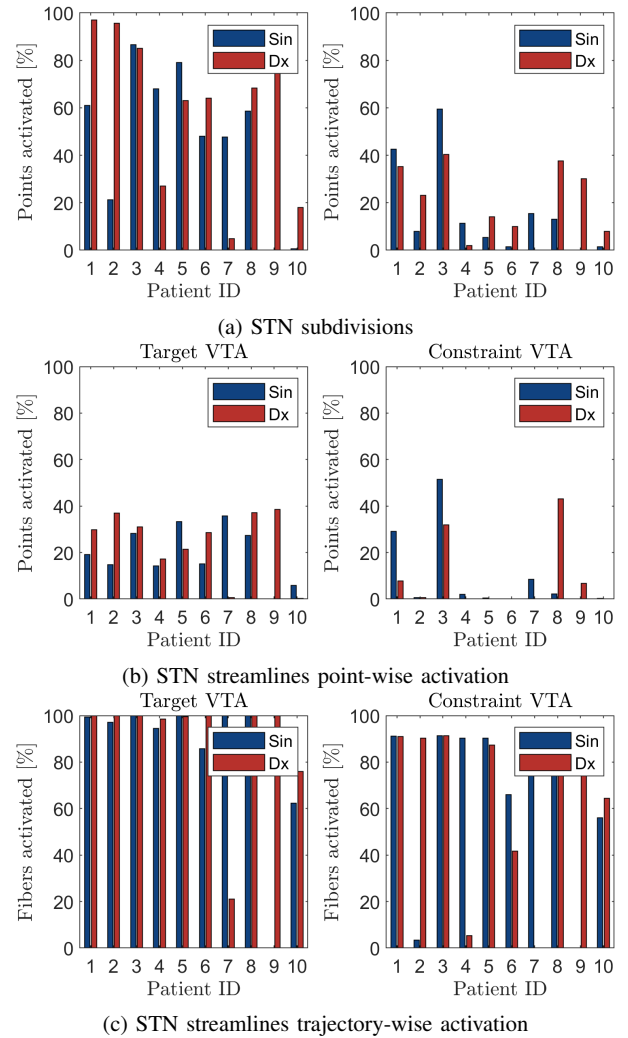


Fig. 4: Target and constraint coverage for clinical settings: (a) the STN subdivisions, (b) point-wise activation of the STN streamlines, and (c) trajectory-wise streamline activation of the STN streamlines.

Fig. 5 illustrates the distribution of VTA volume allocated to target and constraint regions for both STN subdivisions and STN streamlines in clinical settings. The volumes were calculated using MATLAB's built-in function *alphaShape*, with target and constraint VTA expressed as a percentage of the total VTA volume. Notably, the distribution for the STN subdivision target VTA appears relatively uniform and lacking a distinct peak, whereas a clear peak can be observed for the STN streamlines. This peak may indicate that a consistent, albeit small, portion of the stimulation volume should be allocated to the STN motor streamlines for symptom alleviation.

B. Optimal contact configurations

The following section presents the contact configuration suggestions produced by solving optimization problems (3) and (5) for the individualized models in TuneS. The results presented in Fig. 6 and Fig. 7 indicate that the two optimization schemes yield similar results, when applied to the same set of targets and constraints. Although the linear algorithm is quicker, both optimization schemes are efficiently solvable on a standard computer.

In the following, the sensitivity of the optimal solutions to variations in the constraint relaxation variable γ , as well as the impact of the chosen targets and constraints on the predicted configurations, are explored in more detail.

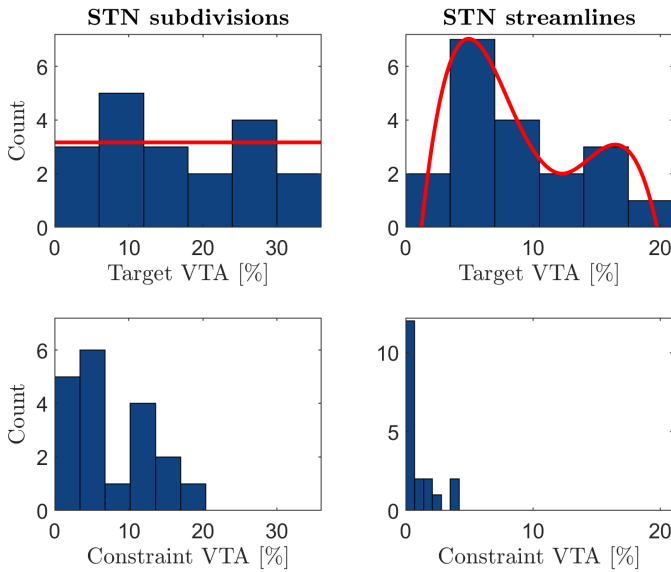


Fig. 5: Distribution of the VTA allocated to target and constraint regions for both STN subdivisions and STN streamlines under clinical settings. The target and constraint VTA are presented as percentages of the total VTA volume, thereby representing the relative allocation of stimulation. Top left plot – the red line is a fit to uniform distribution; Top right plot – the red line is the bimodal distribution fitted by spline.

a) Robustness analysis: To assess the consistency of the recommendations for both optimization schemes, Fig. 6 illustrates how frequent each individual contact appears in the top suggested contact combinations as the relaxation parameter γ is varied from 0 to 90 percent. Additionally, the effect of the constraint variable γ on the ranking score is given in Fig. 7. Both the linear and nonlinear optimization schemes yield comparable results, achieving similar scores and showing consistent behavior for the individual DBS leads. A notable difference occurs at larger γ values, where the nonlinear optimization stabilizes at a consistent score due to penalization for overstimulation. This penalization effectively limits the stimulation amplitude, thereby providing a measure for patient safety, irrespective of the ranking coefficients.

The top suggested settings that were ranked highest with respect to (6) are given in Table A1 and Table A2 for the linear and the nonlinear optimization scheme, respectively.

b) STN subdivisions vs streamlines: The results in Fig. 6 highlight that targeting the STN streamlines, as opposed to its subdivisions, results in more recommendations for dorsally positioned contacts (higher along the z -axis) as well as more combinations involving vertically adjacent contacts. Further, it can be observed that much lower scores for targeting the streamlines compared to the STN subdivisions are reported in Fig. 7. This is a result of the point-wise computation of target coverage in the optimization scheme. For the STN subdivisions, the maximum achieved scores vary strongly, with both leads of Patient 10 standing out for achieving the lowest scores overall. This behaviour is not observed for the STN streamlines, where the results are more consistent, indicating constraint relaxation has less influence on the overall score.

C. Comparison *in silico*

The contact and amplitude predictions by TuneS are based on a fixed pulse width and frequency, which corresponds to the selected VTA threshold. For a retrospective comparison *in silico*, the TuneS contact suggestions were compared to the clinically active settings

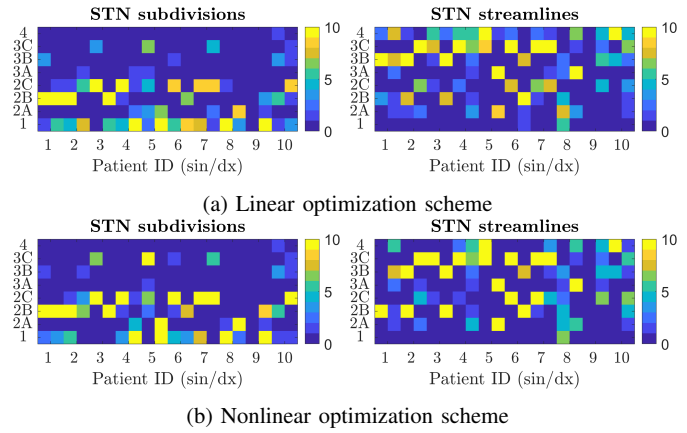


Fig. 6: Counts of contacts in the top-ranked suggestions for (a) the linear optimization scheme in (3) and (b) the nonlinear optimization scheme in (5), across constraint relaxations ranging from 0 to 90%. A count of zero (dark blue) means the contact was not included in any top-ranked configuration, while a count of ten (yellow) indicates that the respective contact consistently appeared in the top-ranked combination across all relaxation levels.

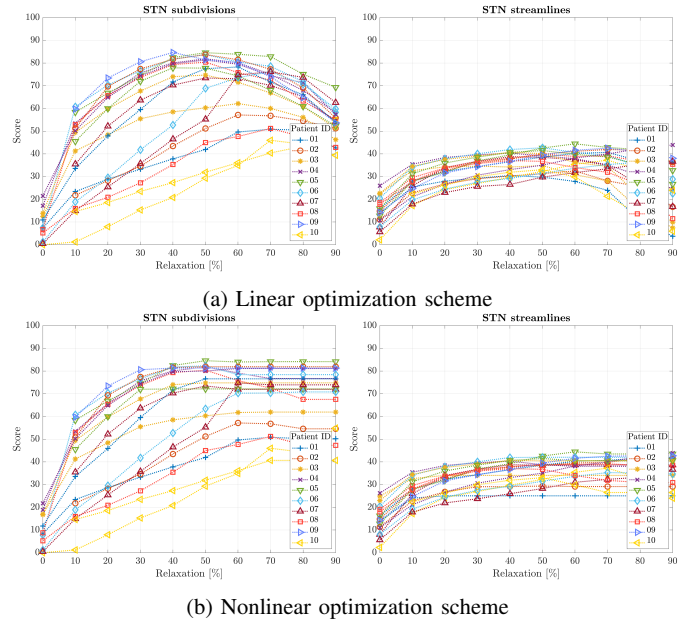


Fig. 7: Effect of constraint relaxation on target coverage and the ranking score given by (6) for a) the linear optimization scheme in (3) and b) nonlinear optimization scheme in (5).

using the clinically active amplitude and pulse width adjusted electric field norm thresholds [24]. The corresponding Dice-Sørensen's scores of the respective VTAs are given in Fig. 8.

For both the STN subdivisions and the streamlines, high Dice-Sørensen's scores between settings predicted by TuneS and clinical settings were achieved when considering the entire VTA and the target volume. Notably, a perfect match ($D = 1$) with clinically used contact configurations was achieved by TuneS for the left lead in Patient 6 when targeting STN subdivisions. Similarly, a perfect match was observed for the right lead in Patient 6 when targeting STN streamlines. However, low Dice scores were observed for the VTA comparison in the constraint volume. Nevertheless, this discrepancy is explainable by very low or zero constraint coverages for the TuneS suggestions at clinical amplitude (cf. Fig. 4b) and is therefore

not indicative of major differences between clinical and suggested settings.

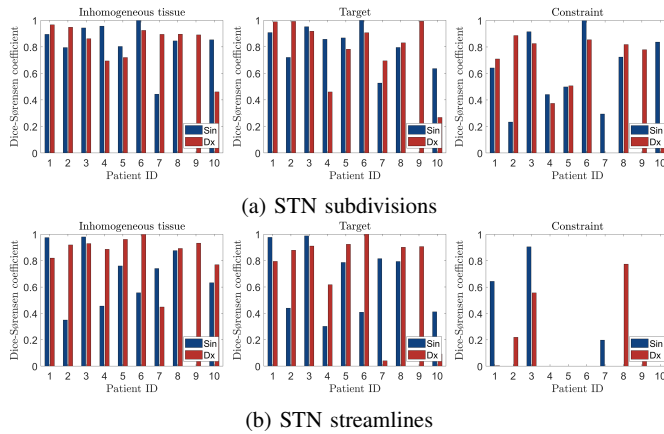


Fig. 8: Dice-Sørensen’s scores of VTAs comparing clinical settings and TuneS suggestions choosing (a) the STN subdivisions or (b) the STN streamlines as targets and constraints. From left to right, the entire VTA, the VTA covering the target, and the VTA covering the constraint region are compared.

As illustrated in Fig. 7, Patient 10 consistently achieved the lowest scores compared to the rest of the cohort. Specifically, for the left lead, TuneS was unable to identify a configuration that provided adequate target coverage while maintaining an amplitude below the safety constraint of 10 mA. These findings align with the challenges faced during clinical programming sessions for this patient, which required frequent adjustments, and can be attributed to the lead’s position, which is relatively far from the target structure, as depicted in Fig. 9(b). Notably, the lead position shifted substantially between the CT scan taken three days post-surgery (i.e. Fig. 9(a)) and the one taken several months later, due to air entering the skull during surgery, Fig. 9(b).

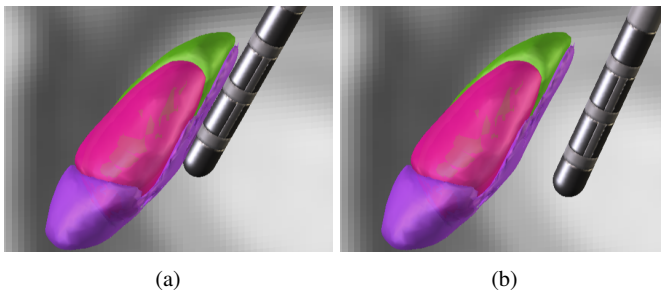


Fig. 9: Reconstruction of the left lead for Patient 10 using a CT (a) with air in the skull, taken three days after surgery, and (b) without air, taken several months later. A significant shift of the lead position relative to the STN subdivisions can be observed. Notably, the DBS lead is positioned outside of the STN motor in both cases.

IV. DISCUSSION

The results presented in this paper are related to only one of the potential neuromodulation applications of TuneS. The pipeline is however not limited to a single disorder and can be employed to explore stimulation targets in a wide variety of those.

A. Clinical settings

Clinically used settings typically provide satisfactory symptom relief, yet they do not necessarily constitute ground-truth of the optimal

configuration. Moreover, clinical settings typically do not elicit any side effects and, therefore, are not expected to impose on constraint regions rather than achieve optimal target coverage. Thus, proving the therapeutical superiority of one contact configuration over another requires clinical validation supported by symptom quantification. In PD, objective quantification of symptoms and stimulation induced side-effects remains a challenge but is, for the time being, addressed by e.g. smartphone and smartwatch applications, eye tracking, and motion detectors [25], [26].

B. Optimal contact configurations

a) Robustness analysis: In clinical settings, all three segmented contacts A, B, C in one row (see Fig. 2) are often used, whereas the use of individual segmented contacts is usually explored when the former settings do not yield a satisfying effect. In contrast, the automated algorithm typically favors a single contact or a combination of two segmented contacts to avoid spill from contacts that are distant from the target. It should be noted, that although just two optimization problems are investigated in this paper, additional cost functions for different targets and constraints may be implemented in TuneS by the user.

Furthermore, different contact configurations often perform similarly in simulation and are therefore ranked closely. Therefore, as mentioned above, proving the efficiency of one combination over another requires clinical testing.

b) STN subdivisions vs streamlines: The choice of targets and constraints strongly influences the prediction of the optimal contact configuration. In particular, targeting the STN streamlines typically resulted in more dorsal contact predictions compared to the STN subdivisions, see Fig. 6. The dorsal region of the STN and adjacent white matter have repeatedly been reported as a “sweet spot” in STN DBS [27], [28], leading to motor improvements in larger PD patient cohorts. Given the findings in the present paper, this suggests that STN streamlines may be a more effective target in image-guided programming algorithms than the STN subdivisions themselves. This is in line with recent discoveries of disease- and symptom-specific “sweet streamlines” [29], [30], which could be integrated in TuneS as targets in future models. In particular, symptom-specific streamlines offers potential to tailor the stimulation based on the patient’s specific symptoms.

Although the recommendations by TuneS for optimal contact configurations are generally consistent — often suggesting the same contacts or their immediate neighbors for given targets and constraints — the suggested amplitudes can vary depending on user-defined degrees of freedom in the optimization schemes. These degrees of freedom include the relaxation of the chosen optimization scheme, the VTA threshold, and the selection of the ranking coefficients, cf. (6). As previously reported by [7], safety constraints that produce amplitudes comparable to those used clinically are highly patient-specific and may be influenced by individual factors like tissue conductivity, stimulation sensitivity, and symptom severity. The dynamical stimulation parameters, i.e. pulse length and frequency, also could play a role in the variability.

C. Limitations

The results obtained with TuneS are subject to several limitations, which the user should be well aware of.

First, a simple static model is used for modeling the VTA produced by the DBS lead. The static model neglects dynamic parameters such as frequency and pulse width. Further, it was previously shown that VTAs for bipolar configurations are inadequately represented by VTAs computed from electric field norm thresholds [31]. Consequently, bipolar settings were neglected in this paper. Further,

potential differences in tissue conductivity between patients were neglected by assuming the same conductivity values for GM, WM, and CSF in all patients.

Second, TuneS incorporates the lead orientation obtained from post-operative CT scans, yet the CT scans were taken for clinical purposes and may not always provide the optimal features for the orientation detection algorithm. Depending on the slice thickness and the angle between the slice and the lead axis, reconstructing the lead orientation based on the DBS marker can be difficult. Determining whether the orientation is pointing in one direction or the opposite direction (180 degrees away) is particularly challenging due to the symmetry of the marker artifact. This uncertainty can significantly affect the suggestion of a specific contact segment. However, new photon-counting CT scanners may offer the possibility to very clearly and unambiguously determine lead orientation [32].

Third, the brute-force approach of testing a given number of contact combinations limits computational efficiency, particularly as the number of individual contacts increases with more advanced lead designs. Moreover, this study only considers evenly distributed current across all active contacts, whereas modern pulse generators allow for uneven current distributions, offering greater flexibility in practice.

Lastly, this paper marks the first attempt to include streamlines as both targets and constraints in automated optimization schemes. While point-wise streamline activation proved feasible in this study, trajectory-wise activation offers a more intuitive measure of white matter tract engagement. In this study, large activation of constraint regions were observed for trajectory-wise activation (c.f. Fig 4c), which does not mirror the fact that clinical settings usually do not elicit side-effects. This discrepancy may be attributed to the specific streamlines selected as constraints in this paper. Using disease- or symptom-specific sweet streamlines [29], [30] as targets, along with corresponding “sour streamlines” as constraint regions, may be more conclusive and is left for future research. Nevertheless, trajectory-wise activation introduces binarity, leading to non-smooth activation functions that could result in ill-posed optimization challenges. It is important to note that streamline atlases typically use probabilistic mappings derived from large patient cohorts. As a result, while these streamlines may exhibit general similarities, they do not necessarily match the patient-specific anatomical fibers, and individual responses to stimulation are likely to vary.

A version of TuneS with reduced dependencies, particularly COM-SOL, is a work in progress to enable more users to incorporate TuneS into their workflow. Currently, only atlas-based targets are supported out of the box, but manually defined targets and constraints can be incorporated by the user.

V. CONCLUSION

This paper introduces TuneS, an automated optimization pipeline for DBS settings, demonstrating its value as a research tool for exploring various target and constraint regions. Although the findings presented here are based on a small cohort of Parkinson’s disease patients, TuneS holds promise for application across a range of neurological and mental disorders. Notably, it represents the first attempt to extend automated optimization algorithms to the targeting of streamlines, which have been at a matter of increasing research interest. Nevertheless, several open questions remain, particularly regarding the quantification of streamline activation in a static model and whether the current model complexity is sufficient to explain patient outcomes. To address these challenges, future efforts should focus on integrating simulation results with objective symptom quantification measurements.

TABLE A1: TuneS top suggested settings for the linear optimization algorithm given in 3 for targeting either the STN subdivisions or STN streamlines.

Patient		STN subdivisions		STN streamlines	
		Contacts	I_0 [mA]	Contacts	I_0 [mA]
01	sin	2B,3B	2.5	2B,3B	1.7
	dx	2B	2.9	3B	4.1
02	sin	2B	2.2	2B,3B	2.3
	dx	1,2C	3.1	2C,3C	4.4
03	sin	2C,3C	2.0	3C,4	1.8
	dx	1,2B	2.0	2B,3B	2.2
04	sin	2C	2.3	3C,4	1.7
	dx	1	3.6	2A,3A	6.6
05	sin	2C,3C	3.2	3C,4	3.1
	dx	1,2A	1.7	2A,3A	2.7
06	sin	1,2C	2.4	2C,3C	2.8
	dx	1,2B	3.5	2B,3B	4.7
07	sin	1,2C	2.1	2C,3C	1.9
	dx	2C,3C	4.1	3C,4	4.5
08	sin	1	2.9	1,2A	3.2
	dx	2A	2.7	3A,4	2.0
09	sin	-	-	-	-
	dx	1	2.5	4	4.3
10	sin	2B	6.8	3B,4	4.7
	dx	1,2C	2.7	2C,3B	2.1

TABLE A2: TuneS top suggested settings for the nonlinear optimization algorithm given in 5 for targeting either the STN subdivisions or STN streamlines.

Patient		STN subdivisions		STN streamlines	
		Contacts	I_0 [mA]	Contacts	I_0 [mA]
01	sin	2B,3B	2.5	2B	1.2
	dx	2B	2.3	3B	4.2
02	sin	2B	2.2	3B	2.0
	dx	2B	2.0	2B,3B	2.2
03	sin	2C,3C	2.3	3C	1.1
	dx	2B	1.9	2B,3B	2.2
04	sin	2C	2.3	3C,4	1.7
	dx	1,2A	4.0	2A,3A	6.6
05	sin	2C,3C	3.2	3C,4	3.1
	dx	1,2A	1.4	2A,3A	2.7
06	sin	2C	2.6	2C,3C	2.4
	dx	2B	4.0	2B,3B	4.2
07	sin	1,2C	2.1	2C,3C	1.9
	dx	2C,3C	3.5	3C,4	4.5
08	sin	1	2.9	2A,3A	3.7
	dx	2A	2.7	3A,4	2.0
09	sin	-	-	-	-
	dx	1,2B	2.2	2C,3B	4.9
10	sin	2B	6.8	3B,4	4.7
	dx	2C	2.1	2C,3B	2.1

APPENDIX

ACKNOWLEDGMENT

The computations were enabled by resources provided by the National Academic Infrastructure for Supercomputing in Sweden (NAISS) and the Swedish National Infrastructure for Computing (SNIC) at UPPMAX partially funded by the Swedish Research Council through grant agreements no. 2022-06725 and no. 2018-05973.

REFERENCES

- [1] J. B. Pietzsch, A. M. Garner, and W. J. Marks, Jr, “Cost-Effectiveness of Deep Brain Stimulation for Advanced Parkinson’s Disease in the United States,” *Neuromodulation: Technology at the Neural Interface*, vol. 19, no. 7, pp. 689–697, 10 2016.
- [2] C. R. Honey, C. Hamani, S. K. Kalia, T. Sankar, M. Picillo, R. P. Munhoz, A. Fasano, and M. Panisset, “Deep Brain Stimulation Target Selection for Parkinson’s Disease,” *Canadian Journal of Neurological Sciences / Journal Canadien des Sciences Neurologiques*, vol. 44, no. 1, pp. 3–8, 1 2017.

- [3] V. Chandra, J. D. Hilliard, and K. D. Foote, "Deep brain stimulation for the treatment of tremor," *Journal of the Neurological Sciences*, vol. 435, p. 120190, 4 2022.
- [4] J. L. Ostrem, M. San Luciano, K. A. Dodenhoff, N. Ziman, L. C. Markun, C. A. Racine, C. de Hemptinne, M. M. Volz, S. L. Heath, and P. A. Starr, "Subthalamic nucleus deep brain stimulation in isolated dystonia," *Neurology*, vol. 88, no. 1, pp. 25–35, 1 2017.
- [5] S. Chabardes, P. Krack, B. Piallat, T. Bougerol, E. Seigneuret, J. Yelnik, S. Fernandez Vidal, O. David, L. Mallet, A.-L. Benabid, and M. Polosan, "Deep brain stimulation of the subthalamic nucleus in obsessive-compulsive disorders: long-term follow-up of an open, prospective, observational cohort," *Journal of Neurology, Neurosurgery & Psychiatry*, vol. 91, no. 12, pp. 1349–1356, 12 2020.
- [6] A. Wagle Shukla, P. Zeilman, H. Fernandez, J. A. Bajwa, and R. Mehanna, "DBS Programming: An Evolving Approach for Patients with Parkinson's Disease," *Parkinson's Disease*, vol. 2017, pp. 1–11, 2017.
- [7] R. Cubo, M. Fahlström, E. Jiltsova, H. Andersson, and A. Medvedev, "Calculating deep brain stimulation amplitudes and power consumption by constrained optimization," *Journal of Neural Engineering*, vol. 16, no. 1, 2 2019.
- [8] A. Shub, D. Smith, T. Zesiewicz, T. Malapira, C. Kingsbury, R. Jain, and Y. Bezchlibnyk, "Deep Brain Stimulation Parameter Prediction using GuideXT and Traditional Monopolar Survey in Parkinson's Disease Patients (P8-11.003)," *Neurology*, vol. 98, no. 18-supplement, 5 2022.
- [9] J. Roediger, T. A. Dembek, J. Achtzehn, J. L. Busch, A.-P. Krämer, K. Faust, G.-H. Schneider, P. Krause, A. Horn, and A. A. Kühn, "Automated deep brain stimulation programming based on electrode location: a randomised, crossover trial using a data-driven algorithm," *The Lancet Digital Health*, vol. 5, no. 2, pp. e59–e70, 2 2023.
- [10] P. Sarikhani, B. Ferleger, K. Mitchell, J. Ostrem, J. Herron, B. Mahmoudi, and S. Miocinovic, "Automated deep brain stimulation programming with safety constraints for tremor suppression in patients with Parkinson's disease and essential tremor," *Journal of Neural Engineering*, vol. 19, no. 4, p. 046042, 8 2022.
- [11] S. Wang, G. Zhu, L. Shi, C. Zhang, B. Wu, A. Yang, F. Meng, Y. Jiang, and J. Zhang, "Closed-Loop Adaptive Deep Brain Stimulation in Parkinson's Disease: Procedures to Achieve It and Future Perspectives," *Journal of Parkinson's Disease*, vol. 13, no. 4, pp. 453–471, 6 2023.
- [12] M. J. Connolly, E. R. Cole, F. Isbaine, C. de Hemptinne, P. A. Starr, J. T. Willie, R. E. Gross, and S. Miocinovic, "Multi-objective data-driven optimization for improving deep brain stimulation in Parkinson's disease," *Journal of Neural Engineering*, vol. 18, no. 4, p. 046046, 8 2021.
- [13] J. Aldred, T. Zesiewicz, M. Okun, J. R. Castaneda, L. V. Metman, C. Luca, R. Ramdhani, J. Durphy, Y. Bezchlibnyk, J. Carlson, K. Foote, S. Sani, A. Papanastassiou, J. Jagid, D. Weintraub, J. Piliotis, L. Chen, and R. Jain, "Image-Guided Programming Tool for DBS Programming Used with a Multiple-Source, Constant-Current System Reduces Initial Programming Time (P4-11.012)," *Neurology*, vol. 100, no. 17-supplement_2, 4 2023.
- [14] V. Torres, K. Del Giudice, P. Roldán, J. Rumià, E. Muñoz, A. Cámara, Y. Compta, A. Sánchez-Gómez, and F. Valdeoriola, "Image-guided programming deep brain stimulation improves clinical outcomes in patients with Parkinson's disease," *npj Parkinson's Disease*, vol. 10, no. 1, 12 2024.
- [15] "Created in BioRender. Frigge, A. (2024) BioRender.com/ p51j952."
- [16] A. Horn, N. Li, T. A. Dembek, A. Kappel, C. Boulay, S. Ewert, A. Tietze, A. Husch, T. Perera, W. J. Neumann, M. Reiser, H. Si, R. Oostenveld, C. Rorden, F. C. Yeh, Q. Fang, T. M. Herrington, J. Vorwerk, and A. A. Kühn, "Lead-DBS v2: Towards a comprehensive pipeline for deep brain stimulation imaging," *NeuroImage*, vol. 184, pp. 293–316, 1 2019.
- [17] A. Husch, M. V. Petersen, P. Gemmar, J. Goncalves, and F. Hertel, "PaCER - A fully automated method for electrode trajectory and contact reconstruction in deep brain stimulation," *NeuroImage: Clinical*, vol. 17, pp. 80–89, 2018.
- [18] T. A. Dembek, A. Hellerbach, H. Jergas, M. Eichner, J. Wirths, H. S. Dafsari, M. T. Barbe, S. Hunsche, V. Visser-Vandewalle, and H. Treuer, "DiODE v2: Unambiguous and Fully-Automated Detection of Directional DBS Lead Orientation," *Brain Sciences*, vol. 11, no. 11, p. 1450, 10 2021.
- [19] C. Neudorfer, K. Butenko, S. Oxenford, N. Rajamani, J. Achtzehn, L. Goede, B. Hollunder, A. S. Ríos, L. Hart, J. Tasserie, K. B. Fernando, T. A. K. Nguyen, B. Al-Fatly, M. Vissani, M. Fox, R. M. Richardson, U. van Rienen, A. A. Kühn, A. D. Husch, E. Opri, T. Dembek, N. Li, and A. Horn, "Lead-DBS v3.0: Mapping deep brain stimulation effects to local anatomy and global networks," *NeuroImage*, vol. 268, p. 119862, 3 2023.
- [20] V. Fonov, A. C. Evans, K. Botteron, C. R. Almli, R. C. McKinstry, and D. L. Collins, "Unbiased average age-appropriate atlases for pediatric studies," *NeuroImage*, vol. 54, no. 1, pp. 313–327, 1 2011.
- [21] R. Cubo, M. Astrom, and A. Medvedev, "Electric field modeling and spatial control in Deep Brain Stimulation," in *2015 54th IEEE Conference on Decision and Control (CDC)*. IEEE, 12 2015, pp. 3846–3851.
- [22] S. Ewert, P. Plettig, N. Li, M. M. Chakravarty, D. L. Collins, T. M. Herrington, A. A. Kühn, and A. Horn, "Toward defining deep brain stimulation targets in MNI space: A subcortical atlas based on multimodal MRI, histology and structural connectivity," *NeuroImage*, vol. 170, pp. 271–282, 4 2018.
- [23] E. Middlebrooks, R. Domingo, T. Vivas-Buitrago, L. Okromelidze, T. Tsuboi, J. Wong, R. Eisinger, L. Almeida, M. Burns, A. Horn, R. Uitti, R. Wharen, V. Holanda, and S. Grewal, "Neuroimaging Advances in Deep Brain Stimulation: Review of Indications, Anatomy, and Brain Connectomics," *American Journal of Neuroradiology*, vol. 41, no. 9, pp. 1558–1568, 9 2020.
- [24] M. Åström, E. Diczfalusy, H. Martens, and K. Wårdell, "Relationship between neural activation and electric field distribution during deep brain stimulation," *IEEE Transactions on Biomedical Engineering*, vol. 62, no. 2, pp. 664–672, 2 2015.
- [25] F. Olsson and A. Medvedev, "Nonparametric Time-Domain Tremor Quantification With Smart Phone for Therapy Individualization," *IEEE Transactions on Control Systems Technology*, vol. 28, no. 1, pp. 118–129, 1 2020.
- [26] G. Amprimo, Z. Mei, C. Ferraris, G. Olmo, and D. K. Ravi, "A Data-driven Exploration and Prediction of Deep Brain Stimulation Effects on Gait in Parkinson's Disease," *IEEE Journal of Biomedical and Health Informatics*, pp. 1–13, 2024.
- [27] T. A. Dembek, J. Roediger, A. Horn, P. Reker, C. Oehr, H. S. Dafsari, N. Li, A. A. Kühn, G. R. Fink, V. Visser-Vandewalle, M. T. Barbe, and L. Timmermann, "Probabilistic sweet spots predict motor outcome for deep brain stimulation in Parkinson disease," *Annals of Neurology*, vol. 86, no. 4, pp. 527–538, 10 2019.
- [28] A. de Roquemaurel, T. Wirth, N. Vijaratnam, F. Ferreira, L. Zrinzo, H. Akram, T. Foltynic, and P. Limousin, "Stimulation Sweet Spot in Subthalamic Deep Brain Stimulation - Myth or Reality? A Critical Review of Literature," *Stereotactic and Functional Neurosurgery*, vol. 99, no. 5, pp. 425–442, 2021.
- [29] B. Hollunder, J. L. Ostrem, I. A. Sahin, N. Rajamani, S. Oxenford, K. Butenko, C. Neudorfer, P. Reinhardt, P. Zvarova, M. Polosan, H. Akram, M. Vissani, C. Zhang, B. Sun, P. Navratil, M. M. Reich, J. Volkmann, F.-C. Yeh, J. C. Baldermann, T. A. Dembek, V. Visser-Vandewalle, E. J. L. Alho, P. R. Franceschini, P. Nanda, C. Finke, A. A. Kühn, D. D. Dougherty, R. M. Richardson, H. Bergman, M. R. DeLong, A. Mazzoni, L. M. Romito, H. Tyagi, L. Zrinzo, E. M. Joyce, S. Chabardes, P. A. Starr, N. Li, and A. Horn, "Mapping dysfunctional circuits in the frontal cortex using deep brain stimulation," *Nature Neuroscience*, vol. 27, no. 3, pp. 573–586, 3 2024.
- [30] N. Rajamani, H. Friedrich, K. Butenko, T. Dembek, F. Lange, P. Navrátil, P. Zvarova, B. Hollunder, R. M. A. de Bie, V. J. J. Odekerken, J. Volkmann, X. Xu, Z. Ling, C. Yao, P. Ritter, W.-J. Neumann, G. P. Skandalakis, S. Komaitis, A. Kalyvas, C. Koutsarnakis, G. Stranjalis, M. Barbe, V. Milanese, M. D. Fox, A. A. Kühn, E. Middlebrooks, N. Li, M. Reich, C. Neudorfer, and A. Horn, "Deep brain stimulation of symptom-specific networks in Parkinson's disease," *Nature Communications*, vol. 15, no. 1, p. 4662, 5 2024.
- [31] G. Duffley, D. N. Anderson, J. Vorwerk, A. D. Dorval, and C. R. Butson, "Evaluation of methodologies for computing the deep brain stimulation volume of tissue activated," *Journal of Neural Engineering*, vol. 16, no. 6, 10 2019.
- [32] J. Manfield, S. Thomas, M. Bogdanovic, N. Sarangmat, C. Antoniadis, A. L. Green, and J. J. FitzGerald, "Seeing Is Believing: Photon Counting Computed Tomography Clearly Images Directional Deep Brain Stimulation Lead Segments and Markers After Implantation," *Neuromodulation: Technology at the Neural Interface*, vol. 27, no. 3, pp. 557–564, 4 2024.